EDGE ARTICLE

ROYAL SOCIETY OF CHEMISTRY

Check for updates

All publication charges for this article have been paid for by the Royal Society of Chemistry

Probing substrate binding inside a paramagnetic cavity: a NMR spectroscopy toolbox for combined experimental and theoretical investigation†‡

Sabyasachi Sarkar,[a] Chang-Quan Wu,[b] Santanu Manna,[a] Deepannita Samanta,[a] Peter P.-Y. Chen [ID] *[b] and Sankar Prasad Rath [ID] *[a]

Protein cavities often rely on the paramagnetic metal present in their active site in order to catalyse various chemical transformations in biology. The selective detection and identification of the substrate is of fundamental importance in environmental monitoring and biological studies. Herein, a covalently linked Fe(III)porphyrin dimer-based paramagnetic sensory cavity has been devised for the accurate detection and simultaneous identification of phenol (substrate) binding within the cavity that provides a unique spectroscopic signature with valuable structural and environmental information. These substrates within the paramagnetic cavity leave the fingerprints of the specific binding modes (*exo vs. endo*) which are well distinguished with the help of various spectroscopic studies *viz*. UV-vis, ^{1}H, and ^{19}F NMR and in their respective crystal structures also. The theoretical ^{19}F NMR analysis plays a pivotal role in replicating the observed NMR trends with large chemical shifts of the phenolato species which in turn helps in deciphering the selective binding modes of the phenols and thereby recognizing the chemical environment within the cavity. These findings will help develop an excellent diagnostic tool for *in situ* monitoring of subtle conformational changes and transient interactions.

Introduction

Nature provides us with a rich toolbox of various functional micro- and nano-compartments, *e.g.* lipid vesicles, organelles, protein cages, virus capsids, *etc.* Among them, protein cages/cavities are very special and interesting types of natural nano-compartments due to their unique structural features, robustness and uniform size.[1] These protein cavities often rely on the paramagnetic metal present in their active site in order to catalyse various chemical transformations as observed in the case of cytochrome P450, catalases and peroxidases to name a few.[2] The selective detection and identification of substrates is of fundamental importance in environmental monitoring and biological studies. In this context, the binding of the substrate within the paramagnetic cavity sometimes provides a unique spectroscopic signature (fingerprint) that allows precise and simultaneous identification of such substrate binding in a complex mixture.[3] However, metal complexes possess rich

magnetic resonance properties based on paramagnetic effects of the metal centre and investigation is often complicated and challenging. Therefore, it is highly desirable to develop sensing platforms that provide outputs with effective analyte fingerprints which not only allows an accurate analysis of the complex mixture but also provides valuable structural information.

Binding of the tyrosine moiety to heme is well-known in biology[2] and also in model complexes.[4,5] In this work, a covalently linked Fe(III)porphyrin dimer, that produces a paramagnetic cavity (Fig. 1), has been utilized to investigate preferential binding of several substituted phenols as substrates. Based on the bulk of the substituents, phenols bind either in the *exo–endo* or *exo–exo* fashion. The previous reports by Nolte and coworkers were mainly focused on the host–guest exchange of viologen guests within the porphyrin cage and determination of the binding efficiencies with the help of 1D EXSY measurements[3c] but utilization of paramagnetic NMR as a spectral toolbox to demonstrate the differential binding of the guests remained elusive. Herein we delineate the maiden example of the influence of the paramagnetic metal ion on substrates which has been thoroughly exploited in the ^{1}H and ^{19}F NMR spectral studies to reveal two different chemical environments (*exo vs. endo*) in solution. Moreover, these two modes of binding have been well distinguished using UV-vis spectral studies along with significant differences in the respective structural and geometrical parameters. DFT calculations have played a pivotal role in replicating the experimental

[a]Department of Chemistry, Indian Institute of Technology Kanpur, Kanpur-208016, India. E-mail: sprath@iitk.ac.in

[b]Department of Chemistry, National Chung Hsing University, 145 Xingda Rd., South Dist., Taichung City 402, Taiwan. E-mail: pychen@dragon.nchu.edu.tw
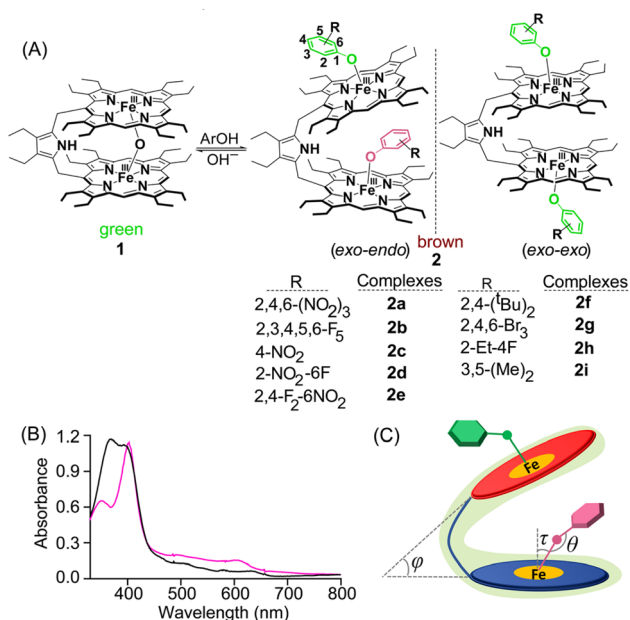
Fig. 1 (A) Synthetic outline of the complexes. (B) UV-vis spectra of **2b** (black) and **2f** (magenta) in CHCl₃ at 298 K and (C) schematic representation displaying critical geometrical parameters upon substrate binding in the *exo–endo* fashion.

^{19}F NMR spectra of the phenolato species that allow precise binding and identification of the substrate inside or outside of the paramagnetic cavity.

Results and discussion

Synthesis

Addition of various phenols into the chloroform solution of pyrrole-bridged μ-oxo porphyrin dimer, **1**, led to the generation of corresponding five-coordinate phenolato species (Fig. 1A). Fig. 1A shows the synthetic outline and the various phenolato complexes reported here along with their abbreviations used.

UV-vis spectroscopy

The preferential mode of binding of various substituted phenols can be differentiated from their respective UV-vis spectra. Taking pentafluoro phenol (Fig. 1B) as a representative example, the corresponding phenolate species **2b** exhibited a split Soret band at 372 and 394 nm along with three Q-bands centred at 504, 584 and 628 nm suggesting the formation of a five-coordinate complex.[4,5] This Soret band splitting is possibly because of the Kasha's exciton coupling of the obliquely arranged chromophores in space.[6] All the complexes having *exo–endo* conformations behaved similarly (Fig. S1‡). In contrast, the phenolate complex with bulky substituents such as 2,4-ditertiarybutylphenol, **2f**, was found to bind in the *exo–exo* fashion having an intense Soret band at 403 nm along with a shoulder at 350 nm and three Q-bands centred at 492, 534 and 610 nm (Fig. 1B). Phenolate species with bulky substituents exhibited similar UV-vis spectral signatures indicating the obvious *exo–exo* binding mode (Fig. S2‡). The UV-vis spectra of

exo–endo and *exo–exo* species are calculated based on time-dependent density functional theory (TD-DFT), which virtually reproduced the experimental spectra of **2b** and **2f** (Fig. S3 and S4‡). The most significant effect was the development of a split Soret band in the case of *exo–endo* and a shoulder for *exo–exo* species (*vide supra*). As shown in Fig. 1B, **2b** has split Soret bands observed at 372 and 394 nm which correspond to HOMO−6 to LUMO+7 (oscillator strength $f \approx 0.37$) and HOMO−5 to LUMO+6 ($f \approx 0.17$), respectively (Fig. S3‡). However, for **2f**, the shoulder and the Soret band observed at 350 and 403 nm are related to HOMO−6 to LUMO+1 ($f \approx 0.69$) and HOMO−2 to LUMO+1 ($f \approx 1.99$), respectively (Fig. S4‡). Thus, UV-vis spectra carry the hallmark of the differential binding of the substrates between *exo–endo* and *exo–exo*.

Crystallographic characterization

Dark brown needle-shaped crystals of **2a**, **2b** and **2f** were grown *via* slow diffusion of *n*-hexane into dichloromethane solutions of the respective complexes in air at room temperature (Fig. 2
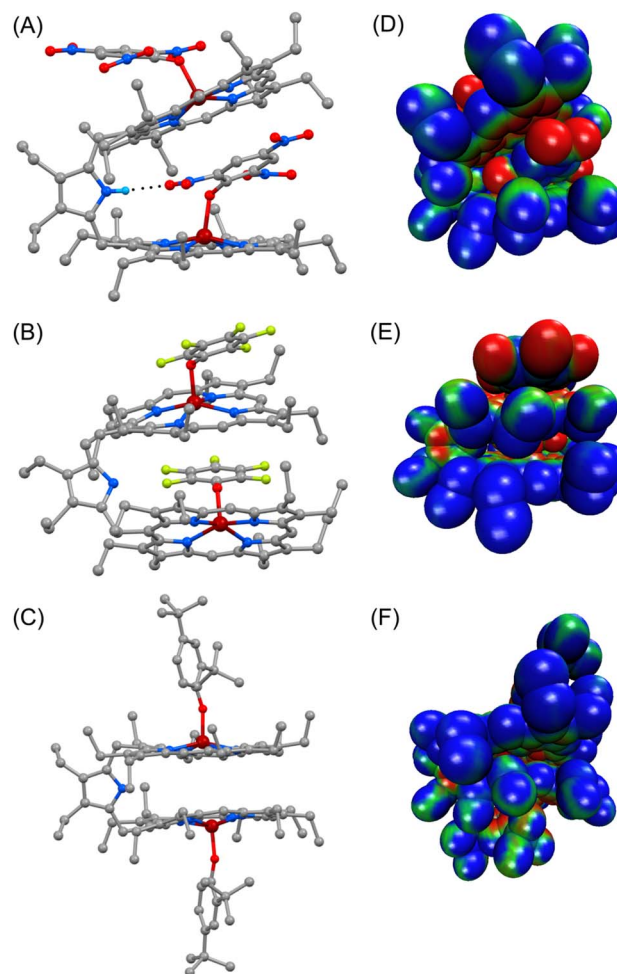

Fig. 2 Perspective views of (A) **2a**, (B) **2b** and (C) **2f** at 100 K (H atoms have been omitted for clarity) (N(H)⋯O distance in **2a** is 2.937(5) Å). Molecular electrostatic potential mapped on the van der Waals surface of (D) **2a**, (E) **2b** and (F) **2f**; electron density is represented on a scale from −0.02 (red) to +0.02 (blue).

and S5–S7‡).[7] All the complexes have two iron centres, each in a five-coordinate square-pyramidal geometry. X-ray structures of **2a** and **2b** clearly display *exo–endo* binding of the substrates, while **2f** demonstrates such binding in an *exo–exo* mode.

Differential binding of the substrate can easily be identified in the structural and geometrical parameters observed in their X-ray structures. The average Fe–N_p distances for **2a** and **2b** are 2.060(3) and 2.062(6) Å for core I and 2.054(3) and 2.055(4) Å for core II, respectively; whereas in the case of **2f** it is 2.071(13) Å (Table 1), which is within the observed range of high-spin ($S = 5/2$) iron(III)-porphyrinates.[8,9] These values are in good accord with the previously reported Fe–N_p distances for axial phenoxide coordinated iron(III)porphyrinates.[4,5] The average Fe–N_p distances of the *endo* phenolate bound Fe(III)porphyrin (core I) is longer than that of the *exo* phenolate bound Fe(III)porphyrin (core II) unit in the cases of **2a** and **2b**.

However, for the *exo–exo* bound species, like **2f**, this distance is much larger. In the case of the *exo–endo* dimer, the *endo*-bound phenolate is sandwiched between two adjacent porphyrins (Fig. 2). Indeed, the *endo*-phenols (C_6 plane) are nearly coplanar with the pophyrinato core (*exo*) having a mean plane separation of 3.15 and 3.09 Å for **2a** and **2b**, respectively, suggesting strong π–π interactions between them. The *endo* binding of the substrate is further facilitated due to the H-bonding interactions between the pyrrolic N–H of the host with the O-atom of the nitro group of the *endo*-bound phenolate in **2a** (Fig. 2A).

An interesting aspect of the differential binding of the substrate is the off-axis tilt angles (Fig. 1C) which are quite different between *exo* and *endo* binding. For example, the *endo* phenolate (7.74°) is much more tilted than the *exo* bound phenolate (0.92°) for **2a** and for **2b** it is 1.56° and 0.10°, respectively. But for the *exo–exo* species **2f**, the value is very small (0.04°). The Fe–O distances observed for **2a** and **2b** are 1.918(3) and 1.874(4) Å for core I, respectively, while for core II the values are 1.911(3) and 1.914(4) Å. But for **2f**, the value is 1.818(13) Å. These values are comparable to the Fe–O distances reported so far for iron(III)porphyrin with phenolato coordination.[4,5] The Fe–O distance has been found to increase with increasing electron withdrawing substituents on the phenols; this is due to the fact that an electron withdrawing substituent with a strong inductive effect (−I) reduces the electron donating

ability of the oxygen atom coordinated to the iron centre, thereby increasing the Fe–O bond length. The Fe–O–C angles for core I and core II are 128.5(2)° and 126.7(3)° in **2a** and 126.6(4)° and 121.9(4)° in **2b**. But for **2f**, the angle is 151.55(11)°. An increase in the Fe–O–C angle leads to an increase in the *s* character of the phenolate oxygen atom leading to the shortening of Fe–O distance. Therefore, **2f** with bulky 2,4-ditertiarybutylphenol having the maximum Fe–O–C angle resulted in the shortest Fe–O distance (Table 1) whereas **2a** shows the longest Fe–O distance due to weaker binding of 2,4,6-trinitrophenol to the Fe(III) centre, owing to the very strong −I effect and resonance (−R) effects of the three electron-withdrawing nitro substituents. Interestingly, the *exo* and *endo* bound phenolate species in the *exo–endo* complexes have very different Fe–O–C angles: the *endo* bound phenols have a larger angle as compared to that of the *exo* bound phenolates (Table S1‡). The trends in structural and geometrical parameters of **2a**, **2b** and **2f** were also found to correlate nicely with the theoretical ones (Table S2‡).

The porphyrin macrocycles in diheme phenolate complexes are highly distorted, while the ring is planar in the related monomeric phenolate complexes (Table 1). As evident, the interaction between two rings in diheme results in larger ring deformation of the individual porphyrin centres. This has also been reflected in the average atom displacements from the mean porphyrin plane (Δ_{24}) and iron displacements therein (Δ_{24}^{Fe}) (Table 1). Notably, in the *exo–endo* complexes, the rings are deformed to different extents. The porphyrin core with the *endo* bound phenolate (core I) is less distorted compared to the porphyrin core with *exo* bound phenolate (core II) (Fig. 4F). The average displacement of atoms from the mean porphyrin plane (Δ_{24}) is 0.08 Å (core-I) and 0.12 Å (core-II) for **2a** and 0.02 Å (core-I) and 0.16 Å (core-II) for **2b** whereas for **2f**, both the cores are equally distorted with a value of 0.12 Å (Fig. S8‡).

The electrostatic potentials have also been mapped onto the van der Waals surface of three representative molecules such as **2a**, **2b** and **2f**, which show quite substantial effects of the phenols in the *exo–endo* and *exo–exo* conformers (Fig. 2D–F). The values of the electrostatic surface potential (ESP) are represented by different colours that vary from red (most negative electrostatic potential) to blue (most positive electrostatic potential); the green part represents the zero-potential regions.

Table 1 Selected structural and geometrical parameters

Complex		Fe–N_p[a]	Fe–O[b]	Fe–O–C[c](θ)	Δ_{24}^{Fe}[d]	Δ_{24}[e]	τ[f]	Φ[g]	Fe⋯Fe[h]	Ref.[i]
2a	Core I (*endo*)	2.060(3)	1.918(3)	128.5(2)	0.46	0.08	7.74	25.89	6.78	tw
	Core II (*exo*)	2.054(3)	1.911(3)	126.7(3)	0.42	0.12	0.90			
2b	Core I (*endo*)	2.062(6)	1.874(4)	126.6(4)	0.39	0.02	1.56	34.79	6.33	tw
	Core II (*exo*)	2.055(4)	1.914(4)	121.9(4)	0.47	0.16	0.10			
2f	*exo*	2.071(13)	1.818(11)	151.55(11)	0.47	0.12	0.04	2.69	6.21	tw
[Fe^{III}(OEP)(2,4,6-(NO$_2$)$_3$OPh)]		2.049(2)	1.930(1)	123.87(12)	0.40	0.02	0.66		—	4c

[a] Averaged value (in Å). [b] Distance (in Å) of the axial ligand. [c] Angle (in °). [d] Displacement (in Å) of iron from the least–squares plane of the $C_{20}N_4$ porphyrinato core. [e] Average displacement (in Å) of atoms from the least–squares planes of $C_{20}N_4$ porphyrinato cores. [f] Tilt-angle (in °). [g] Interplanar angle between the least–square planes of the $C_{20}N_4$ pophyrinato cores (in °). [h] Non-bonding distance (in Å) between two iron(III) centres in a molecule. [i] tw, this work.

For **2a**, the *exo* bound 2,4,6-trinitrophenol moiety induces the charge to the porphyrin ring to a different extent than that of the *endo* bound one (Fig. 2D). In contrast, **2f** with bulky 2,4-ditertiarybutylphenol which prefers *exo–exo* mode of binding exerts very symmetrical charge distribution on two porphyrin rings (Fig. 2F).

^{1}H and ^{19}F NMR spectroscopy

The structure and the properties of these complexes in solution can be obtained from the ^{1}H NMR spectra.[4,8–12] The solid-state structural conformations are also preserved in the solution as is reflected in their respective ^{1}H NMR spectra. The signals are broad and situated in both upfield and downfield regions indicating π-spin delocalization from the Fe(III) centre to the phenolate moiety.[4] The basic resonance pattern of the porphyrin core in the complexes is grossly similar with *meso*-substituted five-coordinate Fe(III)porphyrins of type [XFe^{III}(*meso*-R-OEP)].[4,9,11] Due to extreme broadening of the ^{1}H signals, 2D NMR has not been much informative. It is interesting to compare the ^{1}H NMR spectra between the *exo–endo* and *exo–exo*

Fig. 3 ^{1}H NMR spectra (in CDCl$_3$, at 298 K) of (A) **2c** and (B) **2g**. (C) Schematic representation showing the nomenclature used in ^{1}H NMR peak assignments. Curie plots of the respective *meta* protons of phenoxide are shown in the inset.

conformers taking **2c** and **2g** as two representative examples (Fig. 3A and B).

Highly deshielded methylene (spanning between 31.2 and 44.7 ppm), two downfield shifted bridging signals (at 77.3 and 97.9 ppm), four highly shielded *meso* signals (at −37.5, −41.4, −46.6, and −50.2 ppm), two sets of sharp *meta* signals (at 52.2 and 62.5 ppm) and a very broad *ortho* signal at −78.6 ppm have been observed in the case of **2c**. Methylene peaks appeared between $\delta = 30.1$ and 50.8 ppm in **2g**; however, there have been one set of signals with two *meso* resonances with a 2 : 1 intensity ratio at −54.1 and −59.1 ppm, one bridging signal at 74.2 ppm and one *meta* signal at 70.4 ppm in the complex.

Variable temperature ^{1}H NMR studies have been performed and it was found that two *meta* protons of bound phenolate ions behave very differently in **2c** (Fig. 3A, inset) reflecting the fact that these two signals originated from two different chemical environments which further confirms the intactness of the *exo–endo* conformation in solution, whereas for **2g**, only one set of *meta* signals was found which clearly reflects the symmetrical mode of binding of the phenols in these *exo–exo* species (Fig. 3B, inset). Thus, the behaviour of the *meta* protons serves as a diagnostic tool to discriminate between these two binding modes. A schematic diagram displaying the nomenclature used for ^{1}H NMR peak assignments is shown in Fig. 3C. The ^{1}H NMR spectral behaviours of other *exo–endo* and *exo–exo* complexes are shown in Fig. S9 and S10.‡

In this context, the ^{1}H NMR studies of *monomeric* Fe(III) porphyrins with axial phenolate coordination performed nicely by Arasasingham *et. al.* are worth mentioning.[5e] A series of substitutions varying from electron donating to electron withdrawing groups on the phenolate moiety have been utilized. The ^{1}H NMR spectra of these protoporphyrin (IX) dimethyl esters display spectral features similar to the pattern observed here for the symmetrical *exo–exo* binding mode in which only one set of signals is observed.[5e] In contrast, the ^{1}H NMR spectral investigation of the asymmetrical binding of catechols to the *monomeric* Fe(III) octaethylporphyrins investigated by Rath and coworkers[4d] produced two different sets of *meta*-proton signals similar to the dimeric complexes reported here with *exo–endo* binding mode. In complexes with substituted catechols, the Fe(III) centre can bind either of the two available oxygen atoms of catechol, and hence two sets of downfield shifted *meta*-proton signals are observed in the ^{1}H NMR spectra which reflects the inequivalent mode of binding, a scenario somewhat similar to what we have obtained in the *exo–endo* mode of binding reported here in the dimeric complexes.

The Mulliken spin densities of the phenolate carbon atoms of **2c** are calculated by using DFT, in which the observed spin densities are positive at the *ortho* and *para* positions but are negative at the *meta* position (Fig. S11‡). As a result, the *ortho* and *para* protons are shifted upfield, while the *meta* proton is shifted downfield, as observed in the ^{1}H NMR spectra of the molecules. These contrasting chemical shifts with opposite signs of the spin densities for the *meta* protons *versus* the *ortho/para* protons (Fig. S12‡) are indicative of π-spin delocalization on the phenolate ligand.[4,5c] The temperature dependence of the ^{1}H NMR signals follows the Curie law and a representative

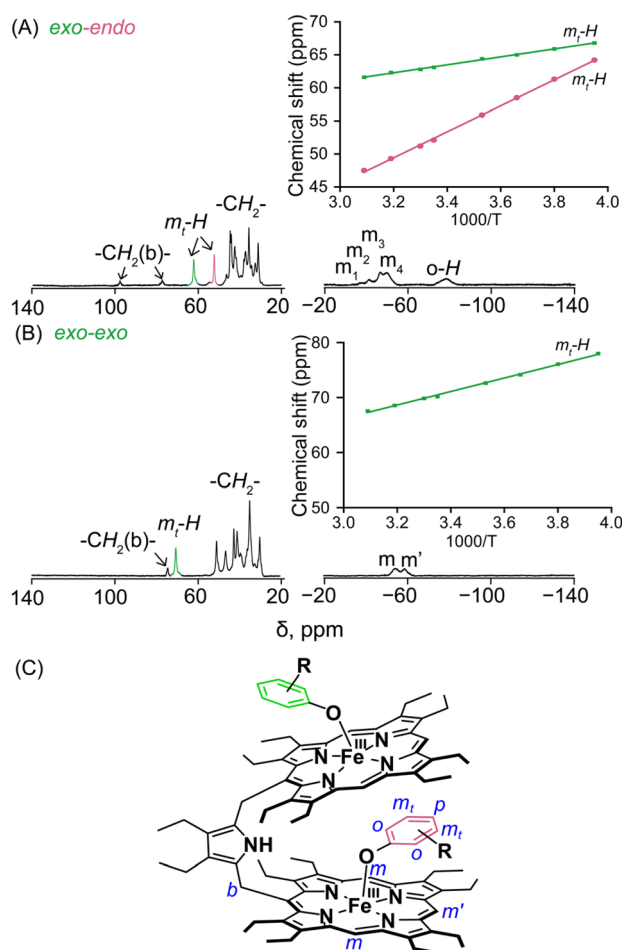example of **2a** has been shown which indicates a single spin state throughout the temperature range (Fig. S13‡).[4,9–12]

^{19}F NMR has been a powerful probe for structural and mechanistic studies due to the presence of the 100% abundant spin 1/2 nucleus with high sensitivity and is particularly attractive for paramagnetic systems in the field of bioinorganic chemistry.[13] The differential binding of the substrate inside and outside the paramagnetic cavity can easily be visualized using ^{19}F NMR also upon using fluorinated substrates in which signals are largely upfield and downfield shifted as demonstrated for **2b**, **2d**, **2e** and **2h** (Fig. S14‡). For **2b**, two sets of *ortho*, *meta* and *para*-F resonances and for **2d** two sets of *ortho*-F signals, owing to *exo–endo* binding, have been observed. The *exo* and *endo* resonances have been assigned by comparing ^{19}F NMR of a series of complexes containing fluorinated substrates along with DFT calculations (*vide infra*). For **2b**, the *ortho*, *para* and *meta*-F signals of the *exo* bound phenol appear at −14.6, 29.7 and −210.2 ppm and for the *endo* bound phenol *ortho*-F resonates at −218.3, 18.7 ppm and *meta*-F appears at

−226.5 ppm. However, *para*-F resonance for *endo* bound phenol was too broad to be detected experimentally. The calculated ^{19}F resonances for **2b** were found to match well with the experimental spectrum (Fig. 4C). Interestingly, the corresponding pentafluorophenolato complex of the *cis*-ethene bridged diiron(III)porphyrin dimer, however, gets stabilized in the *exo–exo* conformation exclusively (Fig. 4D, Scheme S1‡).[4a] In the case of **2d**, two *ortho*-F resonances appear at −28.8 and −171.7 ppm for the *exo* and *endo* bound phenolates, respectively, while **2h** with bulky substituent 2-ethyl-4-fluoro phenol showed only one set of *para*-F resonance which is in sharp contrast to that observed for the *exo–endo* phenols. The *para*-F resonance has been observed at 97.1 ppm for **2h**. Therefore, ^{19}F NMR spectroscopy serves as a powerful tool for distinguishing the *exo–endo* and *exo–exo* modes of binding.

To further confirm the differential behaviour of the *exo* and *endo* [19]F resonances, variable temperature ^{19}F NMR in C_6D_6 was performed for **2b** (Fig. S15‡). As the temperature decreases, the *ortho* and *para*-F resonances of the *exo* bound pentafluoro phenol moiety are increasingly downfield shifted whereas its *meta*-F resonances are shifted in the upfield region. But the *endo* bound pentafluoro phenol gives different ^{19}F resonances: one of the *ortho*-F resonances is increasingly downfield shifted whereas an upfield shift is observed for the other *ortho*-F resonance. The *meta*-F resonance gets increasingly upfield shifted as the temperature decreases.

Estimation of ^{19}F NMR chemical shifts using computational studies

To understand the large upfield and downfield shifts in the ^{19}F NMR spectra, the total NMR chemical shifts (δ_{obs}), eqn (1), including orbital (δ_{orb}), metal-centred dipolar shift (δ_{dip}^{MC}) and contact (δ_{con}) contributions are evaluated using density functional theory (DFT) mentioned below (detailed in the ESI‡).[14,15]

$$\delta_{obs} = \delta_{orb} + \delta_{dip}^{MC} + \delta_{con} \tag{1}$$

By incorporating DFT calculations alongside NMR analysis of **2b** (see details in the ESI‡), it is observed that the orbital shifts and contact shifts demonstrate similarities for the corresponding fluorine atoms in both *exo*-phenol and *endo*-phenol positions, as shown in Table 2. The contact term is highly dependent on the magnitude of the electron magnetic moment positioned at the nucleus, as expressed by eqn (2) in which A_{iso} is the hyperfine coupling constant, γ_I is the gyromagnetic ratio of the nucleus I, g_{iso} is the isotropic g factor of the spin system and μB is the Bohr magneton. In addition, two methods are usually used to evaluate the dipolar shift, namely the metal-centred point-dipole approximation, eqn (3),[14c] and the derivation of the anisotropic part of the hyperfine tensor from electronic structure calculation, eqn (4),[14h] where θ indicates the angle between the metal-nucleus (N) vector and the main axis (z-axis), Φ represents the angle between the projection of the iron-F vector on the xy plane and the x-axis, r refers to the distance between the metal and the nucleus, g_{ani} means the anisotropic part of the g-tensor, and A_{dip} is the dipolar part of the hyperfine coupling tensor.

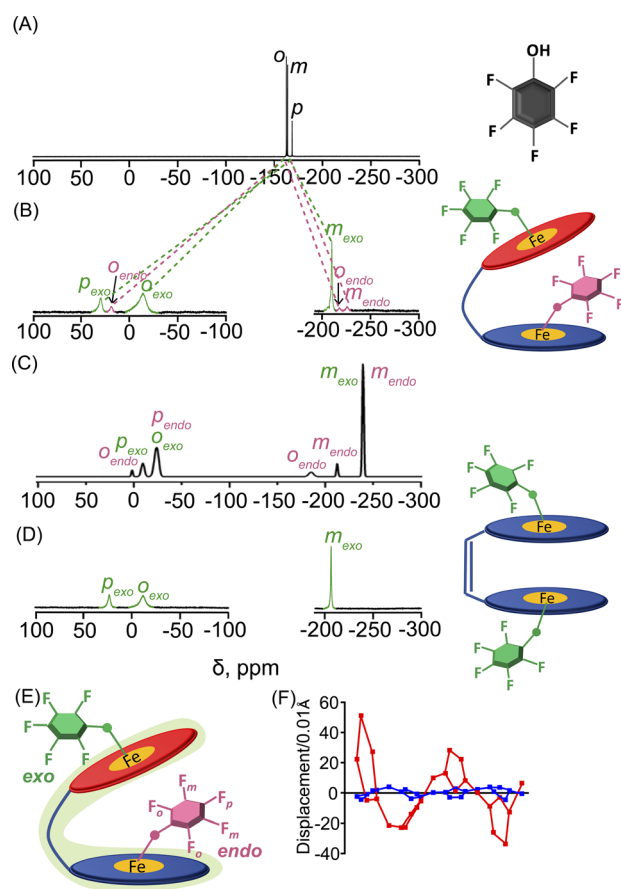**Fig. 4** ^{19}F NMR spectra (at 298 K in C_6D_6) of (A) free pentafluoro phenol and (B) **2b**. (C) DFT calculated ^{19}F NMR spectrum of **2b**. (D) ^{19}F NMR spectrum (in $CDCl_3$ at 298 K) of the pentafluorophenolato analogue of the *cis*-ethene bridged diiron(III)porphyrin dimer (*exo–exo* form, Scheme S1‡). (E) Schematic representation of the *exo–endo* conformer upon pentafluoro phenol binding. (F) Out-of-plane displacement of the porphyrin core atoms of **2b** from the least–squares plane of the $C_{20}N_4$ porphyrinato core. The horizontal axis represents the bond connectivity between atoms.

Table 2 Experimental and DFT calculated ^{19}F NMR data of **2b**

ppm	o-F	m-F	p-F
Experimental			
δ_{obs} (exo)[a]	−14.6	−210.2	29.7
exo-Phenol			
δ_{orb}[b]	−135.6 (−137.2, −134.0)	−152.0 (−154.7, −149.3)	−151.0
δ_{con}[c]	99.1 (62.3, 135.9)	−86.6 (−85.3, −87.8)	170.3
$\delta_{\text{dip}}^{\text{MC}}$ (Fe$_{exo}$)[d]	21.9 (55.0, −11.2)	−3.3 (12.9, −19.5)	−4.8
δ_{obs}[e]	−14.6	−241.9	14.5
$\delta_{\text{M}}^{\text{PC}}$[f]	−11.5 (−5.8, −17.1)	1.1 (−2.5, 4.6)	−22.5
δ_{obs}[g]	−48.0	−237.5	−3.2
endo-Phenol			
	o-F(1), o-F(2)	m-F(1), m-F(2)	p-F
δ_{orb}	−137.1, −133.7	−157.2, −158.7	−153.2
δ_{con}	60.6, 151.0	−65.9, −93.7	184.6
$\delta_{\text{dip}}^{\text{MC}}$ (Fe$_{endo}$)[h]	−67.8, 24.8	24.6, 8.5	−9.5
$\delta_{\text{dip}}^{\text{MC}}$ (Fe$_{exo}$)[h]	−39.8, −17.6	−11.7, 8.1	−27.0
δ_{obs}[i]	−184.1, 24.5	−210.2, −235.8	−5.1
$\delta_{\text{M}}^{\text{PC}}$[j]	−107.1, −14.7	2.4, 31.9	−55.6
δ_{obs}[k]	−183.6, 2.6	−220.7, −220.5	−24.2

[a] Experimental data (at 298 K) assigned for exo-phenol of **2b**. [b] Averaged orbital shift. [c] Averaged contact shift within the exo-phenol. [d] Averaged dipolar shift within the exo-phenol according to eqn (3). [e] $\delta_{\text{obs}} = \delta_{\text{orb}} + \delta_{\text{con}} + \delta_{\text{dip}}^{\text{MC}}$ (Fe$_{exo}$). [f] Averaged dipolar shift within the exo-phenol according to eqn (4). [g] $\delta_{\text{obs}} = \delta_{\text{orb}} + \delta_{\text{con}} + \delta_{\text{M}}^{\text{PC}}$. [h] Dipolar shift within the endo-phenol corresponding to Fe$_{endo}$ and Fe$_{exo}$, respectively, according to eqn (3). [i] $\delta_{\text{obs}} = \delta_{\text{orb}} + \delta_{\text{con}} + \delta_{\text{dip}}^{\text{MC}}(\text{Fe}_{endo}) + \delta_{\text{dip}}^{\text{MC}}(\text{Fe}_{exo})$. [j] Dipolar shift within the endo-phenol according to eqn (4). [k] $\delta_{\text{obs}} = \delta_{\text{orb}} + \delta_{\text{con}} + \delta_{\text{M}}^{\text{PC}}$.

$$\delta_{\text{con}} = \frac{S(S+1)\mu_{\text{B}}}{3\gamma_I kT} g_{\text{e}} A_{\text{iso}} \quad (2)$$

$$\delta_{\text{dip}}^{\text{MC}} = \frac{\mu_0}{4\pi} \frac{\mu_{\text{B}}^2 S(S+1)}{18kT} \frac{1}{r^3} \left[\left(2g_{\text{zz}}^2 - g_{\text{xx}}^2 - g_{\text{yy}}^2\right)(3\cos^2\theta - 1) + 3\left(g_{\text{xx}}^2 - g_{\text{yy}}^2\right)\sin^2\theta \cos 2\phi \right]; \quad (3)$$

$$G_{\text{axial}} = \frac{1}{r^3}\left[(3\cos^2\theta - 1)\right];$$

$$G_{\text{rhombic}} = \frac{1}{r^3}\left[3\sin^2\theta \cos 2\phi\right];$$

$$\delta_{\text{M}}^{\text{PC}} = \frac{S(S+1)\mu_{\text{B}}}{9\gamma_I kT} T_r\left[g_{\text{ani}} A_{\text{dip}}\right] \quad (4)$$

Drawing upon DFT-calculated A_{iso} values obtained from the optimized **2b** structure, it's evident that exo-phenol's rotation in solution is not considered. Remarkably, a substantial difference in contact shifts is observed for the two ortho-fluorine atoms (62.3 and 135.9 ppm), while the two meta-fluorine atoms exhibit comparable values (−85.3 and −87.8 ppm). Conversely, this disparity is evident in both the o-F and m-F configurations of endo-phenol within the same computational analysis, with o-F values of 60.6 and 151.0 ppm and m-F values of −65.9 and −93.7 ppm. However, if we acknowledge that exo-phenol can rotate freely in solution due to the lack of steric hindrance, involving rotations of both its Fe–O and O-Ph single bonds, all chemical shift components for ortho- and meta-fluorine atoms can be averaged, respectively. In contrast, the endo-phenol, being positioned inside the cavity created by two Fe(III) porphyrin units along with a pyrrole-bridge, is no longer able to rotate freely in solution. Consequently, unlike the scenario with exo-phenol, the various components of the chemical shifts cannot be averaged.

Likewise, it could be posited that the spatial orientation of phenol will also significantly influence the dipolar shift. Unlike the contact shift, the dipolar shifts for the fluorine atoms in exo-phenol are primarily influenced by its Fe$_{exo}$ centre. In contrast, endo-phenol is situated in close proximity to both Fe centres (Fe$_{endo}$ and Fe$_{exo}$), resulting in all fluorine atoms experiencing dipolar shifts originating from them. This dipolar shift, as defined in eqn (3), can be evaluated using the G_{axial} and G_{rhombic} factors, along with the g values specified in the text. The corresponding G_{axial} and G_{rhombic} structural factors for the fluorine atoms in exo- and endo-phenols are illustrated in Table S3.‡ It is noteworthy that, when considering their respective coordinated Fe(III) centres, the G_{axial} and G_{rhombic} factors for both exo- and endo-phenols exhibit similarities. Unlike the exo-phenol, the non-coordinating iron centre (Fe$_{exo}$) significantly impacts the G_{axial} and G_{rombic} factors of the endo-phenol as well. Thus, as indicated by eqn (3), the total G factors for fluorine atoms in endo-phenol consistently far exceed those in exo-phenol. Consequently, their dipolar shifts are expected to exhibit notable distinctions, except when the values of both $2g_{\text{zz}}^2 - g_{\text{xx}}^2 - g_{\text{yy}}^2$ and $g_{\text{xx}}^2 - g_{\text{yy}}^2$ approach zero.

After comparing the total G_{axial} and G_{rhombic} factors for both *exo*- and *endo*-phenols in Table S3,‡ significant positive increases were observed in the G_{axial} differences for all *o*-F (27.17 and 16.45), *m*-F (6.97 and 13.51), and *p*-F (8.06) atoms for the *endo*-phenol. These differences contributed to chemical shifts with either all positive or all negative values dependent on the value of $2g_{zz}^2 - g_{xx}^2 - g_{yy}^2$. Notably, a distinct difference in values from positive to negative was observed only for *o*-F atoms (4.62 and −13.78) on G_{rhombic}, which will also result in positive and negative dipolar shifts with $g_{xx}^2 - g_{yy}^2$.

Utilizing the fitting *g* values ($g_{xx} = 2.10$, $g_{yy} = 1.94$, and $g_{zz} = 1.99$) as described in the ESI,‡ the expressions $2g_{zz}^2 - g_{xx}^2 - g_{yy}^2 = -0.2534$ and $g_{xx}^2 - g_{yy}^2 = 0.6464$ were derived. These *g* values in conjunction with the G_{axial} and G_{rhombic} factors in eqn (3) are applied to the dipolar shifts of *exo*- and *endo*-phenol, respectively. The dipolar shifts of *exo*-phenol at *o*-F atoms, 55.0 and −11.2 ppm, exhibit a notable difference, yet these values are averaged (21.9 ppm) to accommodate permissible rotation. Additionally, the averaged dipolar shift of the two *m*-F atoms is −3.3 ppm, and for the single *p*-F atom, it is −4.8 ppm, as depicted in Table 2. In comparison to its contact shift, the dipolar shift contributes a small amount to the paramagnetic shift. Comparing the dipolar shifts calculated using eqn (4), all these values indicate similarly small impacts on the paramagnetic shift as well. Specifically, they are −11.5 ppm (*o*-F), 1.1 ppm (*m*-F), and −22.5 ppm (*p*-F). For *endo*-phenol with restricted orientation, the dipolar shifts are revealed as follows: −107.6 ppm (−67.8 ppm from Fe$_{endo}$ and −39.8 ppm from Fe$_{exo}$) and 7.2 ppm (24.8 ppm from Fe$_{endo}$ and −17.6 ppm from Fe$_{exo}$) for the two *o*-F atoms, respectively. Comparatively, for the two *m*-F atoms, one exhibits a dipolar shift of 12.9 ppm (24.6 ppm from Fe$_{endo}$ and −11.7 ppm from Fe$_{exo}$), while the other displays a shift of 16.6 ppm (8.5 ppm from Fe$_{endo}$ and 8.1 ppm from Fe$_{exo}$). The dipolar shift for the *p*-F atom is −36.5 ppm (−9.5 ppm from Fe$_{endo}$ and −27.0 ppm from Fe$_{exo}$). Notably, the magnitude of the overall dipolar shift in *endo*-phenol surpasses that of *exo*-phenol only when considering the influence of Fe$_{exo}$.

In accordance with the previously discussed orbital shifts, contact shifts, and dipolar shifts, the overall chemical shifts of the two *o*-F atoms in *endo*-phenol exhibit considerable separation. Specifically, one of them is observed at 24.5 ppm, but the other resonance is noteworthy for its extreme upfield position at −184.1 ppm. In contrast, the *m*-F and *p*-F atoms exhibit resonances comparable to those of *exo*-phenol, with the *m*-F resonating in the upfield region and the *p*-F resonating in the downfield region, as illustrated in Fig. 5.

The parallel scenario is observed in the DFT-calculated NMR spectra for the *mono*- and disubstituted fluorophenols within the *exo*–*endo* dimers, particularly (**2d**) and (**2e**), as depicted in Fig. 6. The top panel of Fig. 6A displays the calculated ^{19}F NMR spectrum of **2d** considering a potential free rotation for both *exo*- and *endo*-phenol. This spectrum displays only downfield chemical shifts similar to those observed in the *o*-F atoms of the *exo*-phenol of **2b** (−40 to −70 ppm). Conversely, when considering that the phenol within the *endo*-monomer is anchored between two porphyrin rings, akin to the configuration observed in the *endo*-phenol of **2b**, the calculated NMR peak of
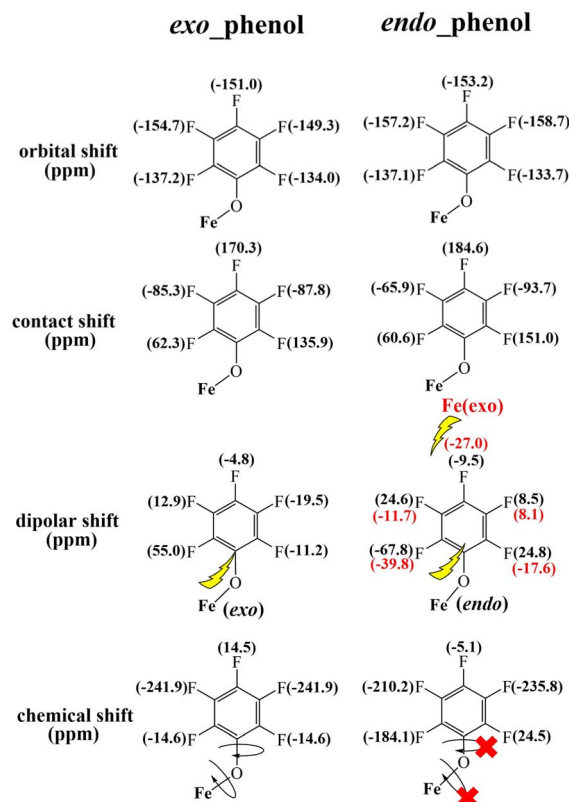

Fig. 5 DFT-calculated orbital and contact shifts along with dipolar shifts for the *exo*–*endo* dimer **2b**.

the *o*-F (*endo*) reveals at −165 ppm. This spectrum notably aligns closely with the experimental distribution, depicted in the lower panel of Fig. 6A.

In the computational analysis of **2e**, assuming free rotation for both *exo*- and *endo*-phenol, the upper panel of Fig. 6B shows an overlap between the *o*-F (*endo*) and *o*-F (*exo*) peaks, located at approximately −80 ppm, with two closely situated *p*-F peaks (*endo* and *exo*) observed around 10 ppm. Nevertheless, this pattern deviates from the experimental results. Similar to **2b** and **2d**, only when *endo*-phenol is anchored in a preferred orientation while allowing unrestricted rotation of *exo*-phenol does the resulting ^{19}F NMR spectrum replicate the distinctive upfield-downfield signals observed experimentally, as depicted in the lower panel of Fig. 6B. The DFT-calculated ^{19}F NMR spectra align seamlessly with the experimental spectra, providing robust support for the assertion that the phenol within the *endo*-monomer is securely positioned between two porphyrin rings in solution (Fig. 6C and D).

In addition, Fig. 7A demonstrates that the fluorine atoms in both *exo*- and *endo*-phenol of **2b** exhibit similar total spin densities. This suggests that the transfer of the high-spin iron centre to phenol through bonds is identical for both configurations. However, the real impact on the chemical shift arises not directly from these spin densities, but from the spin density on the nuclear centre, represented by $(\psi_0^2(\alpha) - \psi_0^2(\beta))$. It is important to note that the nuclear spin density is significantly
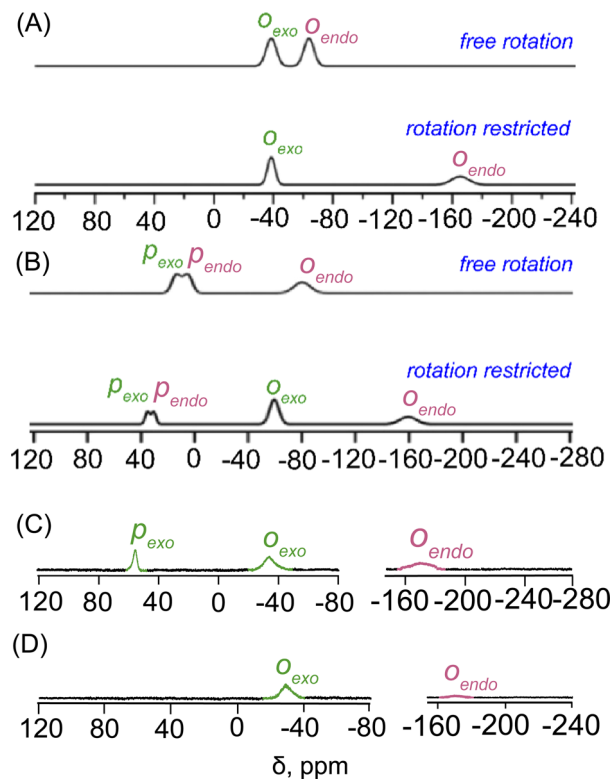
Fig. 6 DFT calculated ^{19}F NMR spectra of (A) the single o-F substituted phenol exo−$endo$ dimer **2d** and (B) the o- and p-F substituted exo−$endo$ dimer **2e** (the upper panel in each case represents spectra with phenols capable of free rotation, while the lower panel depicts the scenario where $endo$-phenol is held in a preferred orientation inside the cavity), and experimental ^{19}F NMR spectra (at 298 K in CDCl$_3$) of (C) **2d** and (D) **2e**.

reduced from the total spin density and may exhibit different anisotropies due to respective spin polarization.

This anisotropy leads to anisotropic hyperfine constants (A_{xx}, A_{yy}, and A_{zz}). The averaged hyperfine value, $A_{iso} = (A_{xx} + A_{yy} + A_{zz})/3$, determines the magnitude of the contact shift, as shown in eqn (2). Generally, atoms with similar total spin densities have similar A_{iso}. Therefore, when the dipolar shift is disregarded, the chemical shifts for exo- and $endo$-phenols are quite close. This approach is commonly adopted for most ^{1}H NMR of paramagnetic species as those protons are relatively far from the metal centre.[14,15] However, deviations in the hyperfine constants from A_{iso} result in noticeable differences in NMR chemical shifts, as described by eqn (4). Even a slight change in anisotropy can lead to a significant difference in dipolar shifts due to the spin (S). Fig. 7B highlights the distinct anisotropies of the two o-F atoms, with the size and shape of the ellipsoid representing their hyperfine tensors. This difference in anisotropy explains the observed dipolar shift differences. Magnetic field lines proposed to be induced by the spin densities of the two iron atoms are depicted in Fig. 7C.

To get more insights about the contributions of steric hindrance in the axial phenoxide complexes, geometry optimizations of **2b** and **2f** have been performed in exo−exo, exo−$endo$ and $endo$−$endo$ conformations. It has been observed that in the

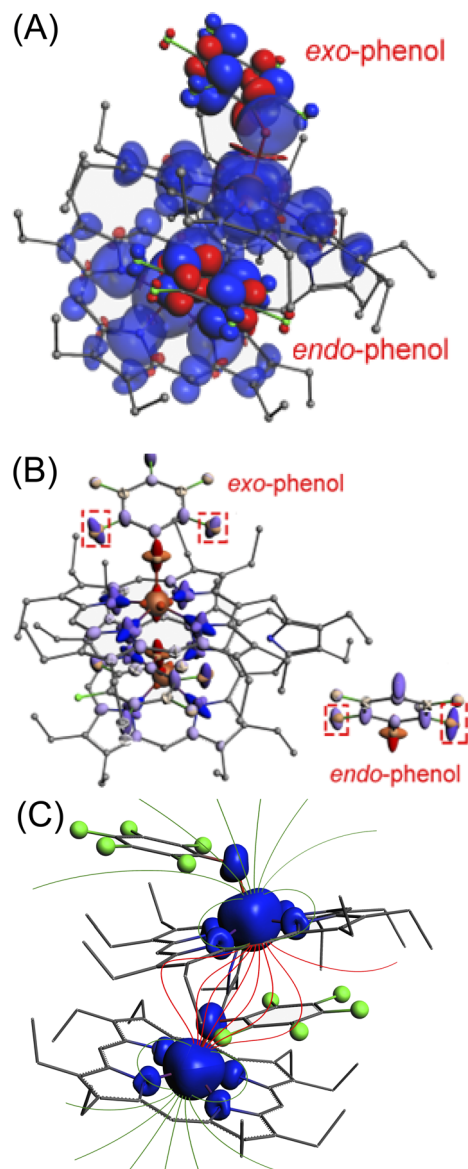**Fig. 7** (A) Spin density of the exo-$endo$ dimer obtained for **2b** using the ZORA-scalar-BP86/TZ2P (COSMO/CH$_2$Cl$_2$) level of theory. The spin density of exo- and $endo$-phenol is highlighted in enhanced solid colour, with other areas displayed at 50% transparency (blue: positive density; red: negative density). (B) Hyperfine coupling tensor of exo−$endo$ dimer **2b**, with the red dotted box highlighting the anisotropic differences of the two o-F atoms in exo-F and $endo$-F, respectively (clamp eigenvalues = 3). (C) A pictorial demonstration displaying differential magnetic fields induced by the spin densities of two iron centers on the exo and $endo$ substrates.

case of **2b** which has smaller substituents around the periphery of the phenolato moiety, the exo−$endo$ conformation was found to be more stable compared to $endo$−$endo$ and exo−exo modes by 15.0 and 17.0 kcal mol^{-1}, respectively in the solution phase (Fig. S16A‡). Contrastingly, for **2f** with bulky substituents such as the 2,4-ditertiarybutyl group on the phenol, the exo−exo conformer was found to be the most stable followed by exo−$endo$ and $endo$−$endo$ conformers (Fig. S16B‡). Phenols containing bulky substituents stabilize the exo−exo conformation whereas,

for smaller substituents, the *exo–endo* conformation is found to be more stable (Fig. S16‡).

Conclusions

An intricate account of structural and spectroscopic study stated here helps discriminate between different axial phenoxide binding inside and outside a paramagnetic cavity created using a pyrrole-bridged Fe(III)porphyrin dimer. The UV-vis, ^{1}H and ^{19}F NMR spectroscopies display very characteristic features in deciphering the phenolato binding in the *exo–endo* and *exo–exo* modes. The behaviours of the *meta* protons in the ^{1}H NMR spectra serve as a crucial tool in discriminating two different types of binding modes. Moreover, the ^{19}F NMR spectra play a pivotal role in identifying substrate binding inside or outside of the paramagnetic cavity with large chemical shifts and thereby recognizing the chemical environment of the cavity. NMR studies also reveal that the solid-state conformations remain unaltered in solution. Complexes with bulky substitution led to the stabilization of the *exo–exo* conformation whereas with smaller substituents *exo–endo* conformation is the favoured mode of binding. Computational calculations reproduce the experimentally observed modes of binding in these complexes also. These findings pave the way for making an excellent probe to develop a diagnostic tool for monitoring subtle conformational changes and transient interactions.

Data availability

The data supporting this article have been included as part of the ESI.‡

Author contributions

S. P. R. conceptualized and supervised the work and wrote the paper along with other coworkers. S. S., S. M. and D. S. performed all the experiments and some of the DFT calculations. C. Q. W. and P. P.-Y. C. have done the DFT calculations related to ^{19}F NMR. The authors have analysed the results together.

Conflicts of interest

There are no conflicts to declare.

Acknowledgements

Notes and references

1 (a) Y. Hsia, J. Bale, B. S. Gonen, D. Shi, W. Sheffler, K. K. Fong, U. Nattermann, C. Xu, P. S. Huang, R. Ravichandran, S. Yi, T. N. Davis, T. Gonen, N. P. King and D. Baker, *Nature*, 2016, **535**, 136–139; (b) Y.-T. Lai, E. Reading, G. L. Hura, K. –L. Tsai, A. Laganowsky, F. J. Asturias, J. A. Tainer, C. V. Robinson and T. O. Yeates, *Nat. Chem.*, 2014, **6**, 1065–1071; (c) M. Rother, M. G. Nussbaumer, K. Rengglic and N. Bruns, *Chem. Soc. Rev.*, 2016, **45**, 6213–6249; (d) Z. Liu, J. Qiao, Z. Niu and Q. Wang, *Chem. Soc. Rev.*, 2012, **41**, 6178–6194.

2 (a) D. R. Nelson, in *Cytochrome P450: Structure, Mechanism and Biochemistry*, ed. P. R. Ortiz de Montellano, Kluwer Academic/Plenum, New York, 2005, 3rd edn; (b) S. Itoh and H. Fujii, in *Dioxygen-Binding in Metalloproteins and Corresponding Models*, ed. E. C. Constable, G. Parkin and L. Que Jr., Elsevier, Oxford, 2021, p. 200; (c) S. P. de Visser, *Chem.–Eur. J.*, 2020, **26**, 5308–5327; (d) A. R. Baglia, J. P. T. Zaragoza and D. P. Goldberg, *Chem. Rev.*, 2017, **117**, 13320–13352; (e) T. L. Poulos, *Chem. Rev.*, 2014, **114**, 3919–3962; (f) L. Que Jr and W. B. Tolman, *Nature*, 2008, **455**, 333–340; https://pubmed.ncbi.nlm.nih.gov/18800132/-full-view-affiliation-1; (g) Y. Watanabe, H. Nakajima and T. Ueno, *Acc. Chem. Res.*, 2007, **40**, 554–562; (h) W. Nam, *Acc. Chem. Res.*, 2007, **40**, 465; (i) I. G. Denisov, T. M. Makris, S. G. Sligar and I. Schlichting, *Chem. Rev.*, 2005, **105**, 2253–2278; (j) B. Meunier, S. P. de Visser and S. Shaik, *Chem. Rev.*, 2004, **104**, 3947–3980; (k) M. Sono, M. P. Roach, E. D. Coulter and J. H. Dawson, *Chem. Rev.*, 1996, **96**, 2841–2888.

3 (a) J. Novotny, S. Komorovsky and R. Marek, *Acc. Chem. Res.*, 2024, **57**, 1467–1477; (b) A. Swartjes, P. B. White, J. P. J. Bruekers, J. A. A. W. Elemans and R. J. M. Nolte, *Nat. Commun.*, 2022, **13**, 1846–1853; (c) A. Swartjes, P. B. White, M. Lammertink, J. A. A. W. Elemans and R. J. M. Nolte, *Angew. Chem., Int. Ed.*, 2021, **60**, 1254–1262; (d) J. P. J. Bruekers, M. A. Hellinghuizen, A. Swartjes, P. Tinnemans, P. B. White, J. A. A. W. Elemans and R. J. M. Nolte, *Eur. J. Org Chem.*, 2022, e202200111; (e) J. Kretschmer, T. David, M. Dracinsky, O. Socha, D. Jirak, M. Vit, R. Jurok, M. Kuchar, I. Cisarova and M. Polasek, *Nat. Commun.*, 2022, **13**, 3179–3191; (f) M. D. Ward, C. A. Hunter and N. H. Williams, *Acc. Chem. Res.*, 2018, **51**, 2073–2082; (g) J. Chyba, A. Hruzikova, M. Knor, P. Pikulova, K. Markova, J. Novotny and R. Marek, *Inorg. Chem.*, 2023, **62**, 3381–3394; (h) J. Zhang, W. Kosaka, H. Sato and H. Miyasaka, *J. Am. Chem. Soc.*, 2021, **143**, 7021–7031; (i) J. C. Ott, E. A. Suturina, I. Kuprov, J. Nehrkorn, A. Schnegg, M. Enders and L. H. Gade, *Angew. Chem., Int. Ed.*, 2021, **133**, 23038–23046; (j) M. Lehr, T. Paschelke, E. Trumpf, A.-M. Vogt, C. Nather, F. D. Sonnichsen and A. J. A. McConnell, *Angew. Chem., Int. Ed.*, 2020, **59**, 19344–19351; (k) K. Du, D. Zemerov, S. H. Parra, J. M. Kikkawa and I. J. Dmochowski, *Inorg.*

Chem., 2020, **59**, 13831–13844; (*l*) Y. Zhao, G. Markopoulos and T. M. Swager, *J. Am. Chem. Soc.*, 2014, **136**, 10683–10690.

4 (*a*) F. S. T. Khan, S. J. Shah, S. Bhowmik, F. G. C. Reinhard, M. A. Sainna, S. P. de Visser and S. P. Rath, *Dalton Trans.*, 2019, **48**, 6353–6357; (*b*) F. S. T. Khan, A. K. Pandey and S. P. Rath, *Chem.–Eur. J.*, 2016, **22**, 16124–16137; (*c*) S. Bhowmik, S. Dey and S. P. Rath, *Chem.–Eur. J.*, 2013, **19**, 13732–13744; (*d*) A. Chaudhary, R. Patra and S. P. Rath, *Eur. J. Inorg. Chem.*, 2010, 5211–5221.

5 (*a*) P. Campomanes, U. Rothlisberger, M. Alfonso-Prieto and C. Rovira, *J. Am. Chem. Soc.*, 2015, **137**, 11170–11178; (*b*) A. Takahashi, T. Kurahashi and H. Fujii, *Inorg. Chem.*, 2009, **48**, 2614–2625; (*c*) D. Kanamori, Y. Yamada, A. Onoda, T. Okamura, S. Adachi, H. Yamamoto and N. Ueyama, *Inorg. Chim. Acta*, 2005, **358**, 331–338; (*d*) L. Cheng, M. A. Khan, D. R. Powell, R. W. Taylor and G. B. Richter-Addo, *Chem. Commun.*, 1999, 1941–1942; (*e*) R. D. Arasasingham, A. L. Balch, C. R. Cornman, J. S. de Ropp, K. Eguchi and G. N. La Mar, *Inorg. Chem.*, 1990, **29**, 1847–1850.

6 M. Kasha, H. R. Rawls and M. A. El-Bayoumi, *Pure Appl. Chem.*, 1965, **11**, 371–392.

7 Crystal data for **2a**: triclinic, space group $P\bar{1}$, $Z = 2$, $a = 12.778(5)$ Å, $b = 16.435(5)$ Å, $c = 21.845(5)$ Å, $\alpha = 82.660(5)°$, $\beta = 82.881(5)°$, $\gamma = 80.640(5)°$, $V = 4464(2)$ Å^3. $d_{calcd} = 1.325$ g cm^{-3}; $T = 100(2)$ K, goodness of fit on $F^2 = 1.021$; $R_1 = 0.0699$ (for $I > 2\sigma(I)$), wR_2 (all data) = 0.1768. For **2b**: monoclinic, space group $I2/a$, $Z = 8$, $a = 34.122(3)$ Å, $b = 14.8098(17)$ Å, $c = 35.216(4)$ Å, $\beta = 100.218(10)°$, $V = 17514(3)$ Å^3. $d_{calcd} = 1.282$ g cm^{-3}; $T = 100(2)$ K, goodness of fit on $F^2 = 1.013$; $R_1 = 0.0821$ (for $I > 2\sigma(I)$), wR_2 (all data)= 0.2443. For **2f**: monoclinic, space group $C2/c$, $Z = 4$, $a = 24.4285(14)$ Å, $b = 17.2727(14)$ Å, $c = 23.7474(15)$ Å, $\beta = 98.248(3)°$, $V = 9916.5(12)$ Å^3. $d_{calcd} = 1.162$ g cm^{-3}; $T = 100(2)$ K, goodness of fit on $F^2 = 1.061$; $R_1 = 0.0351$ (for $I > 2\sigma(I)$), wR_2 (all data) = 0.0902. CCDC-2357051, 2357052 and 2357053 contain the supplementary crystallographic data of **2a**, **2b** and **2f**, respectively, for this paper.

8 (*a*) W. R. Scheidt, in *The Porphyrin Handbook*, ed. K. M. Kadish, K. M. Smith and R. Guillard, Academic Press, San Diego, 2000; vol. 3, p. 49; (*b*) W. R. Scheidt and C. A. Reed, *Chem. Rev.*, 1981, **81**, 543–555.

9 (*a*) P. Chakraborty, N. Ghosh, N. Awasthi and S. P. Rath, *Chem.–Eur. J.*, 2024, **30**, e202400266; (*b*) D. Lai, F. S. T. Khan and S. P. Rath, *Dalton Trans.*, 2018, **47**, 14388–14401; (*c*) T. Guchhait, S. Sasmal, F. S. T. Khan and S. P. Rath, *Coord. Chem. Rev.*, 2017, **337**, 112–144; (*d*) D. Sahoo, M. G. Quesne, S. P. de Visser and S. P. Rath, *Angew. Chem., Int. Ed.*, 2015, **54**, 4878–4882.

10 (*a*) R. Weiss, A. Gold and J. Terner, *Chem. Rev.*, 2006, **106**, 2550–2579; (*b*) M. Nakamura, *Chem. Rev.*, 2006, **250**, 2271–2294; (*c*) Y. Ling and Y. Zhang, *J. Am. Chem. Soc.*, 2009, **131**, 6386–6388; (*d*) D. Sakow, D. Baabe, B. Bçker, O. Burghaus, M. Funk, C. Kleeberg, D. Menzel, C. Pietzonka and M. Brçring, *Chem.–Eur. J.*, 2014, **20**, 2913–2924.

11 (*a*) H. Kalish, J. E. Camp, M. Stępień, L. Latos-Grażyński, M. M. Olmstead and A. L. Balch, *Inorg. Chem.*, 2002, **41**, 989–997; (*b*) S. P. Rath, M. M. Olmstead and A. L. Balch, *J. Am. Chem. Soc.*, 2004, **126**, 6379–6386.

12 (*a*) I. Bertini, C. Luchinat, G. Parigi and E. Ravera, in *NMR of Paramagnetic Molecules*, Elsevier, Amsterdam, 2017, 2nd edn; (*b*) F. A. Walker, in *Handbook of Porphyrin Science*, ed. K. M. Kadish, K. M. Smith and R. Guilard, World Scientific, Singapore, 2010, vol. 6, p. 1; (*c*) M. Nakamura, in *The Handbook of Porphyrin Science*, ed. Y. Ohgo, A. Ikezaki, K. M. Kadish, K. M. Smith and R. Guilard, Word Scientific, Singapore, 2010, vol. 7, p. 1; (*d*) G. N. La Mar, W. De, W. Horrocks and R. H. Holm, in *NMR of Paramagnetic Molecules*, Academic Press, New York, 1973, p. 694.

13 (*a*) L. Cosottini, S. Zineddu, L. Massai, V. Ghini and P. Turano, *J. Inorg. Biochem.*, 2023, **244**, 112236–112240; (*b*) A. M. Gronenborn, *Structure*, 2022, **30**, 6–14; (*c*) D. Xie, M. Yu, R. T. Kadakia and E. L. Que, *Acc. Chem. Res.*, 2020, **53**, 2–10; (*d*) Y. Huang, X. Wang, Lv. Guohua, A. M. Razavi, G. H. M. Huysmans, H. Weinstein, C. Bracken, D. Eliezer and O. Boudker, *Nat. Chem. Biol.*, 2020, **16**, 1006–1012; (*e*) J. Blahut, L. Benda, J. Kotek, G. Pintacuda and P. Hermann, *Inorg. Chem.*, 2020, **59**, 10071–10082; (*f*) Z. Xu, C. Liu, S. Zhao, S. Chen and Y. Zhao, *Chem. Rev.*, 2019, **119**, 195–230; (*g*) K. L. Peterson, K. Srivastava and V. C. Pierre, *Front. Chem.*, 2018, **6**, 160–180; (*h*) A. E. Thorarinsdottir, A. I. Gaudette and T. D. Harris, *Chem. Sci.*, 2017, **8**, 2448–2456; (*i*) A. A. Kislukhin, X. Hongyan, S. R. Adams, K. H. Narsinh, R. Y. Tsein and E. T. Ahrens, *Nat. Mater.*, 2016, **15**, 662–668; (*j*) I. Tirotta, V. Dichiarante, C. Pigliacelli, G. Cavallo, G. Terraneo and F. B. Bombelli, *Chem. Rev.*, 2015, **115**, 1106–1129; (*k*) C. Belle, C. Béguin, S. Hamman and J.-L. Pierre, *Coord. Chem. Rev.*, 2009, **253**, 963–976.

14 (*a*) A. Kehl, M. Hiller, F. Hecker, I. Tkach, S. Dechert, M. Bennati and A. Meyer, *J. Magn. Reson.*, 2021, **333**, 107091–107101; (*b*) I. Bertini, C. Luchinat and G. Parigi, *Prog. Nucl. Magn. Reson. Spectrosc.*, 2002, **40**, 249–273; (*c*) I. Bertini, C. Luchinat and G. Parigi, *Solution NMR of Paramagnetic Molecules: Applications to Metallobiomolecules and Models*, Elsevier Science Ltd., New York, 2001; (*d*) A. Kehl, I. Bertini, C. Owens, C. Luchinat and R. S. Drago, *J. Am. Chem. Soc.*, 1987, **109**, 5208–5212; (*e*) A. Dei, D. Gatteschi and E. Piergentili, *Inorg. Chem.*, 1979, **18**, 89–93; (*f*) R. J. Kurland and B. R. McGarvey, *J. Magn. Reson.*, 1970, **2**, 286–301; (*g*) G. F. Kokoszka and R. W. Duerst, *Coord. Chem. Rev.*, 1970, **5**, 209–244; (*h*) P. Hrobárik, R. Reviakine, A. V. Arbuznikov, O. L. Malkina, V. G. Malkin, F. H. Köhler and M. Kaupp, *J. Chem. Phys.*, 2007, **126**, 024107–024119; (*i*) A. Borgogno, F. Rastrelli and A. Bagno, *Dalton Trans.*, 2014, **43**, 9486–9496; (*j*) W. C. Isley III, S. Zarra, R. K. Carlson, R. A. Bilbeisi, T. K. Ronson, J. R. Nitschke, L. Gagliardi and C. J. Cramer, *Phys. Chem. Chem. Phys.*, 2014, **16**, 10620–10628; (*k*) A. G. Nobile, D. Trummer, Z. J. Berkson, M. Wörle, C. Copéret and P. A. Payard, *Chem. Sci.*, 2023, **14**, 2361–2368; (*l*)

A. Borgogno, F. Rastrelli and A. Bagno, *Chem.–Eur. J.*, 2015, **21**, 12960–12970.

15 (*a*) C. C. Chen, Y. W. Wu, M. Nakamura, R. J. Cheng, T. H. Tseng and P. P. Y. Chen, *Dalton Trans.*, 2019, **48**, 13820–13833; (*b*) R.-J. Cheng, C.-H. Ting, T.-C. Chao, T.-H. Tseng and P. P.-Y. Chen, *Chem. Commun.*, 2014, **50**, 14265–14268; (*c*) C.-C. Chen and P. P.-Y. Chen, *Angew. Chem., Int. Ed.*, 2012, **51**, 9325–9329.